

Wing Lift Enhancement from Aft Rotor Induced Suction

Richard Healy

PhD Candidate

Farhan Gandhi

Redfern Professor

Center for Mobility with Vertical Lift (MOVE), Rensselaer Polytechnic Institute, New York, USA

ABSTRACT

This study examines the aerodynamic interactions of rotor-wing units in which lifting rotors are mounted below and behind a wing. The rotor-wing units are simulated using CFD, and their performance is compared to isolated rotors and wings in order to understand the interference effects. Simulations are performed using the commercial Navier Stokes solver, AcuSolve[®], with a delayed detached eddy simulation (DDES) model. Rotor-wing units with three wing incidence angles (7° , 10° and 13°) as well as three rotor disk loadings (6, 9 and 12 lb/ft^2) are considered. By simulating the flow and comparing the pressure distribution around an isolated wing to one with the rotor installed, the rotor is seen to introduce a low pressure region that extends over the wing's top surface. The additional rotor-induced suction on the top surface of the wing augments wing lift by up to 134%, and provides some stall mitigation at 13° incidence angle. Suction near the leading edge of rotor-installed wings also counters the nominal wing drag, introducing a net propulsive force on the wing at all incidence angles considered. On the rotor, downwash induced by the wing's bound circulation introduces a rotor thrust deficit up to 10% nominal thrust and torque penalty up to 4% nominal torque. Despite the rotor performance penalties, interactions between the rotor and wing lead to equivalent lift to drag ratio improvements ranging from 47% - 52% over a range of wing angles. As disk loading is increased, the rotor-induced suction strengthens, extending the 66% wing lift increment at 6 lb/ft^2 up to 115% at 12 lb/ft^2 . These results suggest that the interactional aerodynamics associated with mounting a rotor below and behind a wing can introduce enhanced system performance over a range of wing angles and rotor loadings.

INTRODUCTION

In recent years there has been a significant interest in using large multi-rotor eVTOL aircraft for Urban Air Mobility. One of the challenges associated with the modeling, simulation and performance prediction of these aircraft is the complex interactional aerodynamic flow fields of multiple rotors operating in close proximity. Several recent studies have used high-fidelity computations to represent these flows (see for e.g., Refs. 1–8), resulting in valuable physical insights as well as an understanding of beneficial geometries/configurations. One such beneficial configuration is the rotor-blown wing which has been shown to increase lift by using the rotor wake to increase dynamic pressure over the airfoil and potentially keep flow attached at high wing angles of attack.

In the context of propeller driven aircraft, Glauert describes how the slipstream of a propeller will augment the lift and drag of a downstream wing in Ref. 9. Glauert also cites experiments by Fage and Collins which show increased propeller thrust due to the presence of the wings (Ref. 10) and describes how asymmetric wing interference will lead to thrust fluctuations. Later studies by Kroo report up to 6% improved propeller efficiency associated with wing-related swirl recovery (Ref. 11). In terms of wing performance, experiments reported by Veldhuis and Chiamonte et al. as well as simulations by Müller et al., Fischer and Ortun have shown wing lift

and drag increments from the wake of the propeller, and reported further lift increases when the rotor is mounted above the wing (Refs. 12–15).

The performance improvements afforded by rotor-blown wings have been employed and tested on the NASA X-57, which is an all-electric experimental aircraft that has been well-studied and uses a distribution of small propellers along its wing for propulsion. The higher dynamic pressure provided by the propeller wakes passing over the wing has been shown to improve the maximum lift coefficient, allowing for the wing to be sized optimally for cruise (Refs. 16, 17). Studies on other platforms such as the CRC-20 (Ref. 18) have also shown improved wing performance when operating in the wake of a tractor propeller (Refs. 2, 19, 20). Certain eVTOL aircraft may take advantage of this effect during wing-borne cruise, but during low-speed flight, propellers will not be the only source of aerodynamic interaction.

During hover and low-speed flight, many popular eVTOL designs supplement lift with vertically thrusting rotors that are fixed to the wing (Refs. 21–26). In these configurations, aerodynamic interactions between these lifting rotors and the wing can be expected to influence overall system performance. Similar interactions have been observed on tiltrotor platforms, where rotor downwash on a tiltrotor's wing has been shown to induce flow separation and reduce wing lift (Refs. 27–29). Aside from the work on tiltrotor configurations, experiments by Tang et al. on a lifting rotor mounted in-front and above a wing has also revealed degraded wing lift due to rotor-wing aerodynamic interaction in forward

Presented at the Vertical Flight Society's 78th Annual Forum & Technology Display, Ft. Worth, Texas, USA, May 10–12, 2022. Copyright © 2022 by the Vertical Flight Society. All rights reserved.

flight (Ref. 30). While these studies have identified scenarios where interaction aerodynamics degrade performance, some configurations could still provide performance improvements similar to those seen on the rotor-blown wing. Aerodynamic interactions between lifting rotors and wings need to be understood to identify favorable configurations, and the conditions under which performance improvements can be achieved.

The present work uses high fidelity blade-resolved computational fluid dynamics (CFD) to investigate the aerodynamic interactions of lifting rotors positioned in close proximity to a wing. In particular, a rotor mounted below and behind a wing is simulated in order to understand the rotor-wing interactions and test the hypothesis that rotor induced suction will augment wing lift and mitigate flow separation at high wing angles of attack. The performance of the rotor-wing system (with interference) is compared to the performance of an isolated rotor and wing (without interference) and the merits of the rotor installed system are evaluated.

ANALYSIS

Problem Description

Six rotor-wing units are simulated in CFD in addition to three isolated wings and three isolated rotors. The rotor-wing unit, shown in Fig. 1 is comprised of an infinite wing and a rotor positioned below and behind the wing's trailing edge. The wing is made "infinite" by extending it in either direction up to a symmetry plane, thereby emulating many wing/rotor units along a larger wing. In this way, the counter-clockwise spinning rotor is modeled as if two clockwise-spinning rotors were operating on either side of it. In Fig. 1, the would-be position of these adjacent rotors and wing segments (not actually simulated) are shown with dashed outlines.

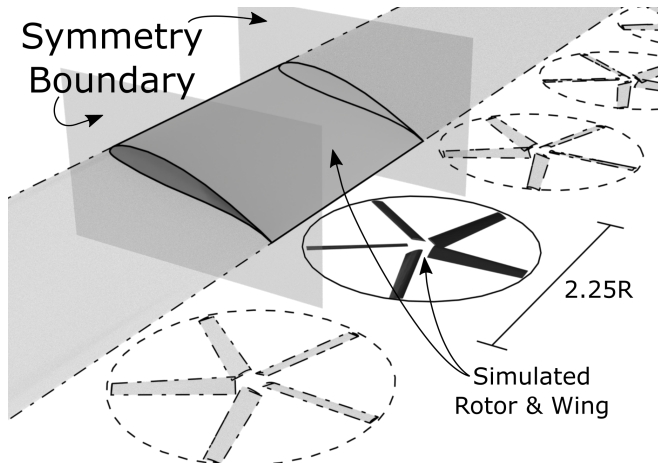


Figure 1: Diagram of the rotor-wing unit, with representations of the adjacent units

The lateral (spanwise) extents of the rotor-wing unit are equal to 2.25 rotor radii ($2.25 R$), leaving $0.25 R$ tip-tip spacing between the rotors. The position of the rotor relative to the wing is shown in Fig. 2, where the distance is measured relative to

the airfoil's quarter chord point. The longitudinal and vertical spacing is chosen to generally match that seen on real world aircraft (Ref. 21) and results in only modest (less than $0.125 R$) longitudinal overlap between the rotor disk and the extents of the wing. The rotor is also mounted low enough to accommodate any wing incidence angle (rotated about the quarter-chord point) without the trailing edge intersecting with the rotor disk.

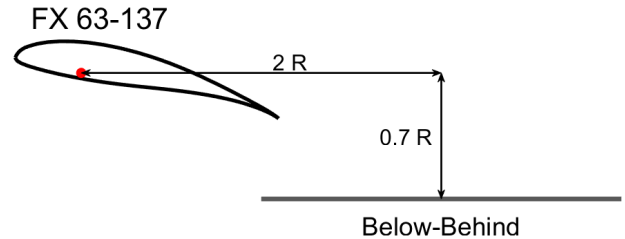


Figure 2: Side view of the rotor-wing unit, with dimensions for the relative rotor position

The rotor parameters, presented in Table 1 are chosen to match the '3 σ 5' rotor presented in Ref. 31. This high solidity, low tip speed rotor design has been shown to produce a relatively weak noise signature which is important for eVTOL vehicles operating in densely populated urban environments. The '3 σ 5' rotor presented in Ref. 31 is scaled to a 2 ft (0.6096 m) radius to better match the scale of wing mounted eVTOL rotors. A representative six rotor and wing system shown in Fig. 3 is used to appropriately size the rotor relative to the wing. Here, the wing chord and aspect ratio are chosen to generally match those seen on winged eVTOL vehicles (3 ft chord, $AR = 9$) (Refs. 21–26). By assuming 6 rotors along the wing, a 1 rotor wide gap in the middle (to accommodate a fuselage) and $0.25 R$ tip-tip rotor spacing, the span of the wing can be related to the rotor radius using $span = 2 \times N_r \times R + N_r \times s$. Here, N_r equals the number of rotors (6), R is the rotor radius and s is the tip-tip spacing. Using this formula, and the selected wing parameters, a rotor radius of 2 ft (0.6096 m) is chosen. For this rotor, blade pitch is held constant and the necessary RPM to match the three target disk loadings (6, 9 and 12 lb/ft²) is found using the Rensselaer Multirotor Analysis Code (RMAC) (Ref. 32), based on blade element theory (BET) with a 3x4 finite state Peters-He inflow representation.

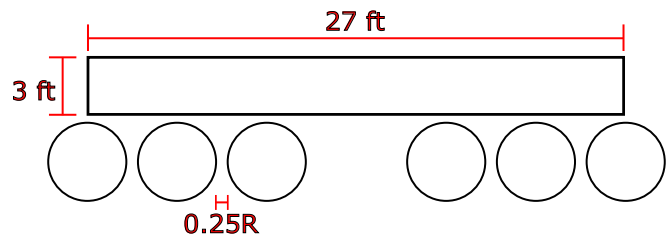


Figure 3: Top view of the system used to determine the rotor radius

refinement region is a second refinement region which is prescribed with elements $\frac{1}{2}$ blade tip chord in size (Fig. 7). This refinement region extends radially $2.0R$ from the rotor hub, extending $1.0R$ above as well as $3.0R$ below the rotor hub, and is angled to accommodate the rotor’s estimated wake skew angle (30.6° at 9 lb/ft^2). A third refinement region with 1 blade tip chord element size has radius $2.5R$ and extends even further downstream of the rotor (Fig. 7). Surrounding the rotor wake refinement regions, an additional mesh refinement zone is prescribed with element size equal to $\frac{1}{10}$ wing chord that extends 5 wing chords from the rotor hub. The entire computational domain is comprised of approximately 48 million elements for wing-rotor cases, with 33 million in the rotating volume, and 15 million in the surrounding non-rotating volume. These rotor mesh parameters have been used in previously published AcuSolve® rotorcraft simulations, and have been found to provide spatial convergence to within 1.2% integrated thrust and 1.6% integrated torque (Refs. 3 and 4).

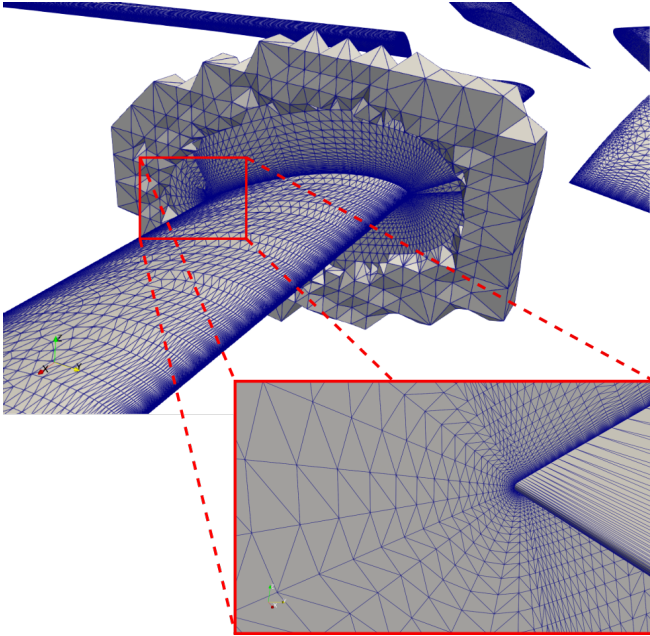


Figure 5: Rotor blade surface mesh as viewed near mid-span and a chordwise slice cutting along the blade showing the boundary layer mesh in the wall-normal direction

A delayed detached eddy simulation (DDES) is used with the Spalart-Allmarus (SA) turbulence model on-body for all simulations. Each case is initially run using time steps corresponding to 10° of rotation for at least 40 revolutions in order to reduce the computational cost of rotor wake development. These initial 10° time steps are possible without numerical divergence due to the stability afforded by the Streamline Upwind Petrov-Galerkin (SUPG) stabilized finite element method and generalized α implicit time integration method. The latter method was designed to suppress high frequency disturbances and allow solution stability with Courant-Friedrichs-Lewy (CFL) number greater than 1 (Refs 38, 39). Following the revolutions simulated with 10° time steps, an additional 5 revolutions (at minimum) are performed

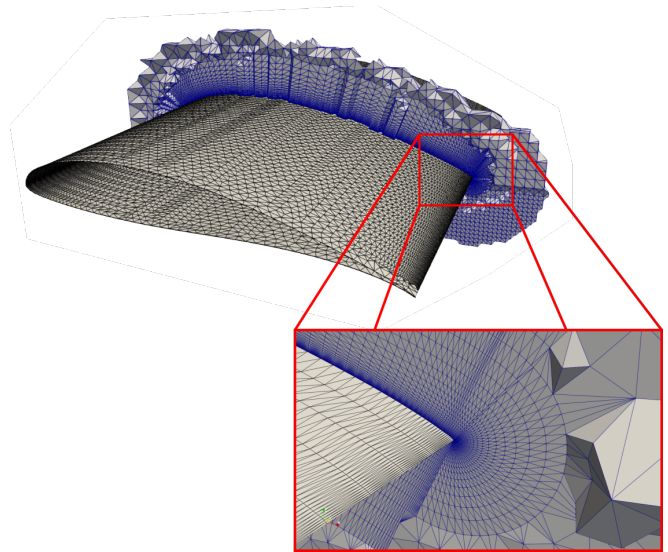


Figure 6: Wing surface mesh as viewed near mid-span and a chordwise slice cutting along the blade showing the boundary layer mesh in the wall-normal direction

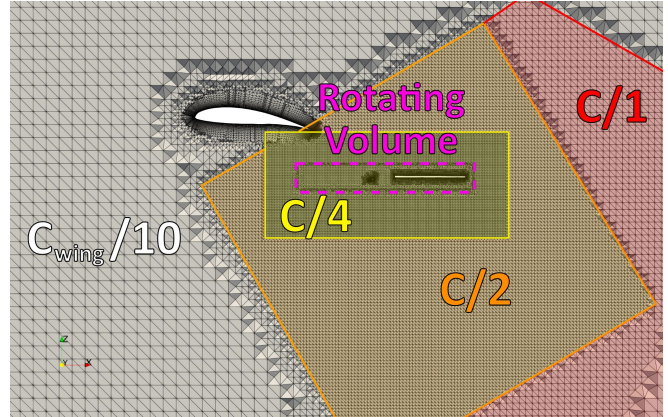


Figure 7: Cross-section of the wake refinement

with time steps corresponding to 1° with sufficient stagger iterations to reduced residuals by two orders of magnitude. If average loads over one revolution are not converged to within 1%, additional revolutions are simulated. All runs are performed on 8 24-core AMD Epyc 7451 processors, part of the Center for Computational Innovations (CCI) at Rensselaer Polytechnic Institute.

Performance Metrics

In order to equally compare the performance of the rotor-wing units, a formulation of the equivalent lift to drag ratio is applied. Using Eq. 1, this single metric can be used to rank the overall merit of a given configuration. Here, L_W and L_R are the lifting force of the wing and rotor respectively. Lifting forces are first normalized by the rotor’s equivalent drag ($Q\Omega/V_\infty + D_R$) where Q is the rotor torque, Ω is the rotor speed, V_∞ is the flight speed and D_R is the rotor H-force. The equivalent rotor drag is then added to the wing drag D_W so that the total lifting forces are normalized by the total drag forces.

In this way, the metric considers how much lifting force is provided for a given unit of power required to spin the rotor and propel the system.

$$\frac{L_{Tot}}{D_{e-Tot}} = \frac{L_W + L_R}{\frac{Q\Omega}{V_\infty} + D_W + D_R} \quad (1)$$

The installation effects of the rotor-wing system are evaluated by comparing the rotor-wing system's overall L_{Tot}/D_{e-Tot} to that of an isolated rotor and wing. The isolated rotor and wing L_{Tot}/D_{e-Tot} is evaluated using the isolated rotor and isolated wing forces. That is, the lift of an isolated wing (in the absence of a rotor) is added to the lift of an isolated rotor (in the absence of a wing) and is normalized by the isolated wing and isolated rotor drag. In this way, the isolated system's L_{Tot}/D_{e-Tot} represents the amount of lift generated per unit of power for a wing-rotor system in which there are no interactional aerodynamic effects.

RESULTS

Overall L_{Tot}/D_{e-Tot}

Three rotor-wing systems are first simulated in which the wing's angle of attack is incremented from 7° to 10° to 13° . For all three cases, the rotor is positioned below and behind the wing (Fig. 3) and operates at a targeted 9 lb/ft^2 disk loading. The overall L_{Tot}/D_{e-Tot} for each case is evaluated (Eq. 1) and compared to an isolated rotor and isolated wing. Fig. 8 presents each system's L_{Tot}/D_{e-Tot} at their respective wing angle of attack.

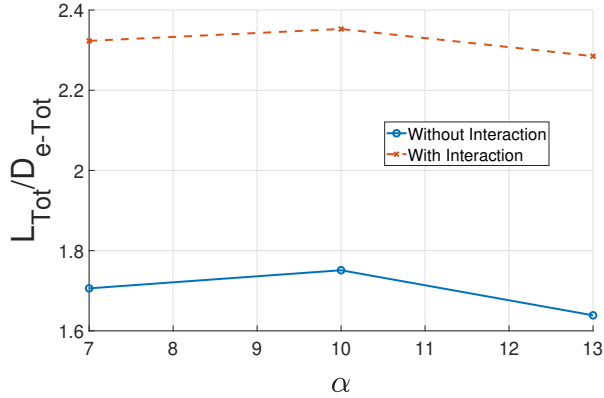


Figure 8: Overall L_{Tot}/D_{e-Tot} vs. angle of attack for rotor-wing units (with interaction) and isolated rotors and wings (without interaction)

For each angle of attack, the rotor-wing unit (with interaction) produces over 34% the L_{Tot}/D_{e-Tot} of the isolated rotor and wings (without interaction). The only difference between the isolated rotor/wing and the rotor-wing system is the inclusion of aerodynamic interactions between the rotor and the wing (flight speed, rotor speed, and rotor/wing orientation are all held constant). This indicates that it is the rotor-wing aerodynamic interactions that are responsible for the performance

improvement. The performance improvement is also insensitive to the wing's angle of attack over this range, and is present when there is no nominal flow separation on the wing. This suggests that the rotor does more than just keep flow on the wing attached, and actually augments the system lift in a more fundamental way.

Wing Performance

One component that is responsible for the L_{Tot}/D_{e-Tot} increment presented in Fig. 8 is changes in the wing lift. Fig. 9 presents the wing's overall lift coefficient at three angles of attack (7° , 10° and 13°) for isolated and rotor-installed wings. Here, the wing lift when the rotor is installed exceeds that of an isolated rotor by up to 200% and is well in excess of the isolated wing's maximum C_L (1.78 as predicted by XFOIL (Ref. 34)). At $\alpha=13^\circ$, the isolated wing lift drops below that at 7° or 10° , indicating the onset of stall at this high angle. For the rotor-installed wing, however, lift continues to rise even at 13° , suggesting that the presence of the rotor does provide some stall mitigation effects as was originally hypothesized.

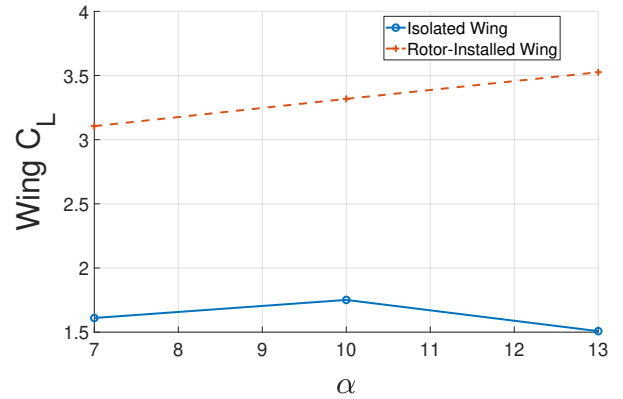


Figure 9: Wing lift coefficient vs. angle of attack for isolated and rotor-installed wings

In order to identify the underlying mechanism for the improved wing lift, the flow field between the rotor and the wing is interrogated. Fig. 10 shows a slice cutting through the center of the 7° isolated wing and rotor-wing unit colored by velocity magnitude as viewed from the side. Here, red represents velocity that is higher than freestream, and blue indicates that the flow is slower than freestream. On the left, the velocity distribution is as expected, with high velocity flow over the top of the wing, and low velocity flow over the bottom of the wing. The flow for the isolated wing appears mostly attached at this relatively low 7° incidence angle. When the rotor is installed, however, the velocity on the top surface of the wing increases by over 5 m/s. Beyond the trailing edge of the wing, the suction induced by the rotor increases the velocity magnitude and pulls the flow partially downwards as indicated by the velocity vectors. The velocity vectors also indicate that inflow into the downstream half of the rotor disk is sourced from flow moving over the top of the wing whereas the inflow

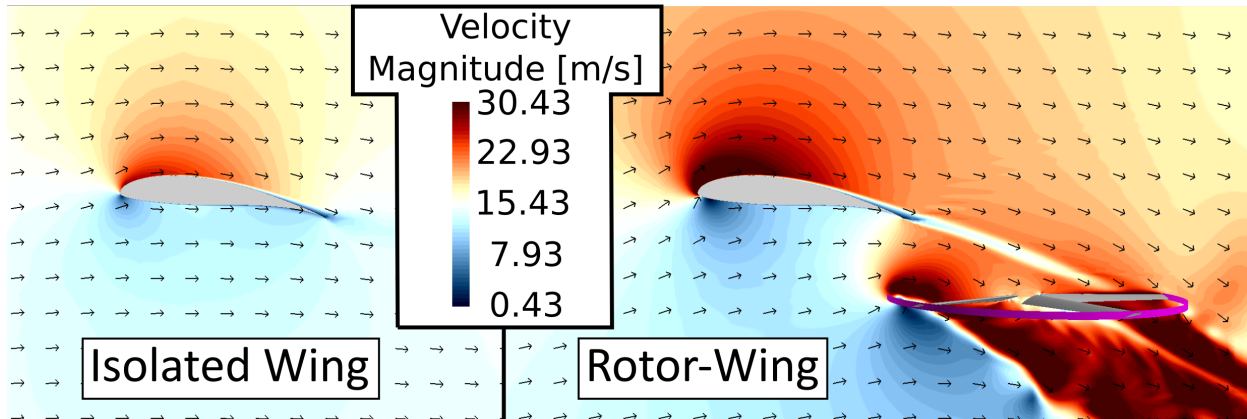


Figure 10: Velocity magnitude slice cutting through the center of an isolated wing ($\alpha=7^\circ$) and rotor-wing unit with velocity vectors

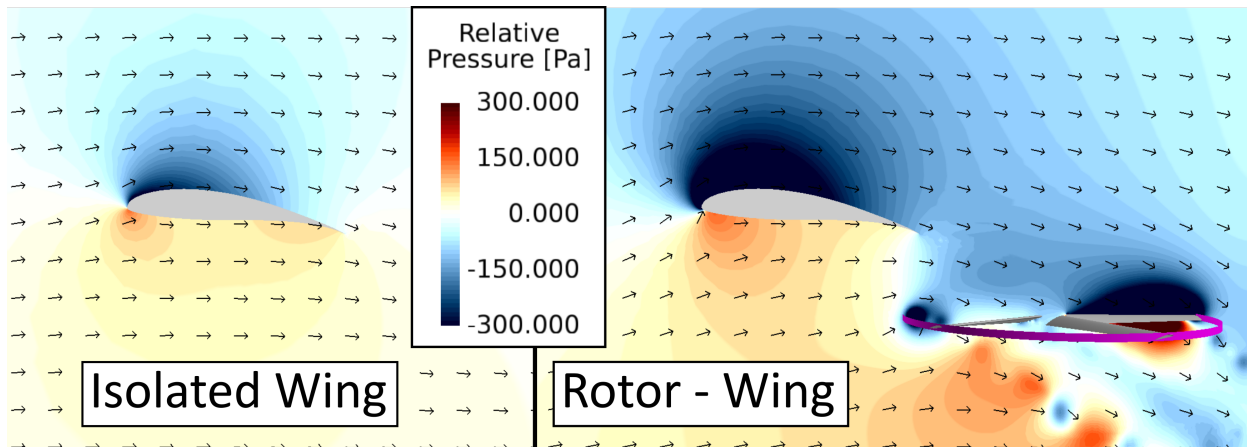


Figure 11: Instantaneous relative pressure slice cutting through the center of an isolated wing ($\alpha=7^\circ$) and rotor-wing unit with velocity vectors

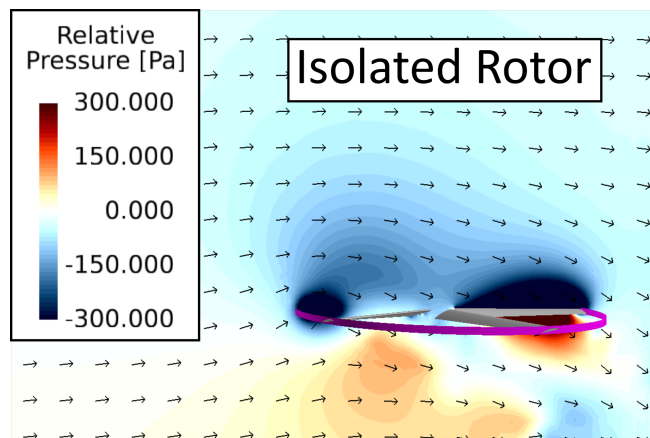


Figure 12: Instantaneous relative pressure slice cutting through the center of an isolated rotor with velocity vectors

at the front of the disk is dominated by flow that had traveled under the wing. Overall, the momentum source generated by the rotor pulls flow over the top surface of the wing before it is ingested into the rotor.

The higher velocity induced by the rotor also corresponds to lower pressure due to Bernoulli's principle. Fig. 11 shows the same slices as in Fig. 10, but colored by instantaneous relative pressure, and Fig. 12 shows the same slice but through an isolated rotor. In Fig. 12, the isolated rotor induces a low pressure region above the rotor disk where inflow is ingested. When this rotor is installed below and behind the wing (as with the rotor-wing system in Fig. 11), this rotor induced suction extends up to the trailing edge of the wing. By comparing the pressure distribution between the isolated wing and the rotor-installed wing, the influence of the rotor can be seen to extend up to the wing's trailing edge, and over the wing's top surface. The pressure is lower on the top surface of the rotor-installed wing, with a larger and generally stronger low pressure region on the front top surface, as indicated by the larger dark blue area. Suction is not induced on the bottom surface of the wing, as indicated by the orange/yellow positive pressure seen under the isolated wing still being present on the rotor-wing system. Therefore, the overall influence of the rotor is over the top surface of the wing where the velocity induced by the rotor drops the relative pressure.

The rotor-induced pressure reduction seen in Fig. 11 can be tied to the increases in wing lift shown in Fig. 9 by investigating the wing's surface pressure. Fig. 13 shows the pressure distribution along the chord of isolated and rotor-installed wings both at 7° incidence angle. Suction over the top surface of the wing is found to be on average about 300 Pa stronger when the rotor is installed, with increases biased towards the leading edge. While some minor suction is imposed on the trailing edges bottom surface, the net effect of the rotor is stronger suction on the top surface of the wing which increases lift to the degree seen in Fig. 9.

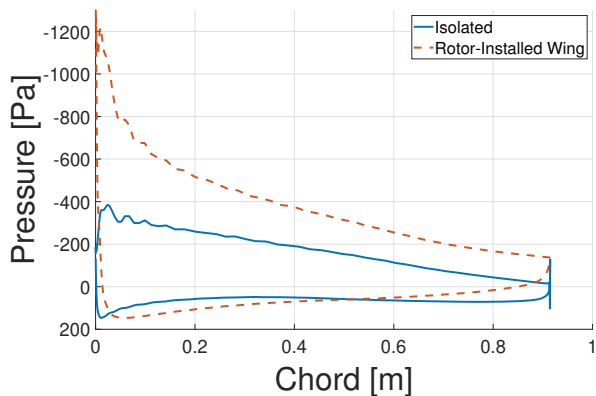


Figure 13: Chordwise relative pressure distribution along an isolated wing and rotor-installed wing at 7° incidence angle

The rotor induced suction seen at 7° wing incidence angle is also present when the wings are at higher angles. Figs. 14 and 15 show the slices in Figs. 10 and 11 respectively when the

rotors are at 10° and 13° . Velocity and pressure contours are similar to those seen in Figs. 10 and 11, with the rotor suction increasing velocity and dropping pressure over the top surface of the wing. At these higher angles of attack however, flow separation on the wing can start to be seen. At 13° wing incidence angle, flow separation is observed on the isolated wing, with dark blue low velocity flow near the trailing edge top surface. Comparing the size of the separation region on the 13° isolated wing to that on the 13° rotor-wing, it appears that the presence of the rotor shrinks the extents of the separated flow. The downwards velocity induced by the rotor over the top of the wing seems to pull down on the flow separation, keeping it more attached to the wing.

The rotor's stall mitigation effects can also be seen in Fig. 16 which shows the pressure distribution of isolated and rotor-installed wings at 7° , 10° and 13° incidence angle. Looking at the pressure distribution of the isolated wing at 13° (plotted in solid green), the suction on the top surface between 0.2-0.7 m chord reduces below that seen at 7° (solid blue) and 10° (solid red). The weakened suction on the top surface of the isolated 13° wing corresponds to the relatively low wing lift shown in Fig. 9. When the rotor is installed (dotted green), the same pressure change is not observed, and the profile remains similar to that of the rotor-installed wings at 7° and 10° (dotted blue and red). The presence of the rotor therefore mitigates stall effects by keeping flow over the top surface more attached and retaining the pressure profile seen at lower incidence angles. By retaining suction on the top surface of the wing, the 13° rotor-installed wing is capable of providing the C_L increment observed in Fig. 9.

In Fig. 16, the presence of the rotor introduces increased suction on the top surface at all three incidence angles. As the incidence angle grows, so too does the strength of the suction near the leading edge and trailing edge. In general, these pressure distributions support the findings presented in Fig. 9, and explain that the source of the lift increase is rotor-induced suction on the top surface of the wing.

The presence of the rotor does not only influence wing lift though. Wing drag is also sensitive to the presence of the rotor as shown in Fig. 17. Here, the wing drag coefficient is plotted versus incidence angle both with and without the rotor installed. Curiously, the wing drag for all rotor-installed wings is negative, indicating that the wing is producing a propulsive force. The strength of this propulsive force reduces with angle of attack, suggesting that this effect is related to how the rotor induced suction is distributed over the wing.

Fig. 18 shows the surface-normal vectors for both the isolated and rotor-installed wings (both at 7°), with the vector lengths scaled by the surface pressure. On the bottom half, only the drag-wise (x-direction) component of the vector is plotted. The combination of suction and normal-direction on the top surface of the isolated wing causes vectors to point partly forwards on the front half of the airfoil (from the leading edge to 39% chord) and point backwards on the aft of the airfoil (39% chord to the trailing edge). The bottom surface is associated with positive pressure and vectors point downstream

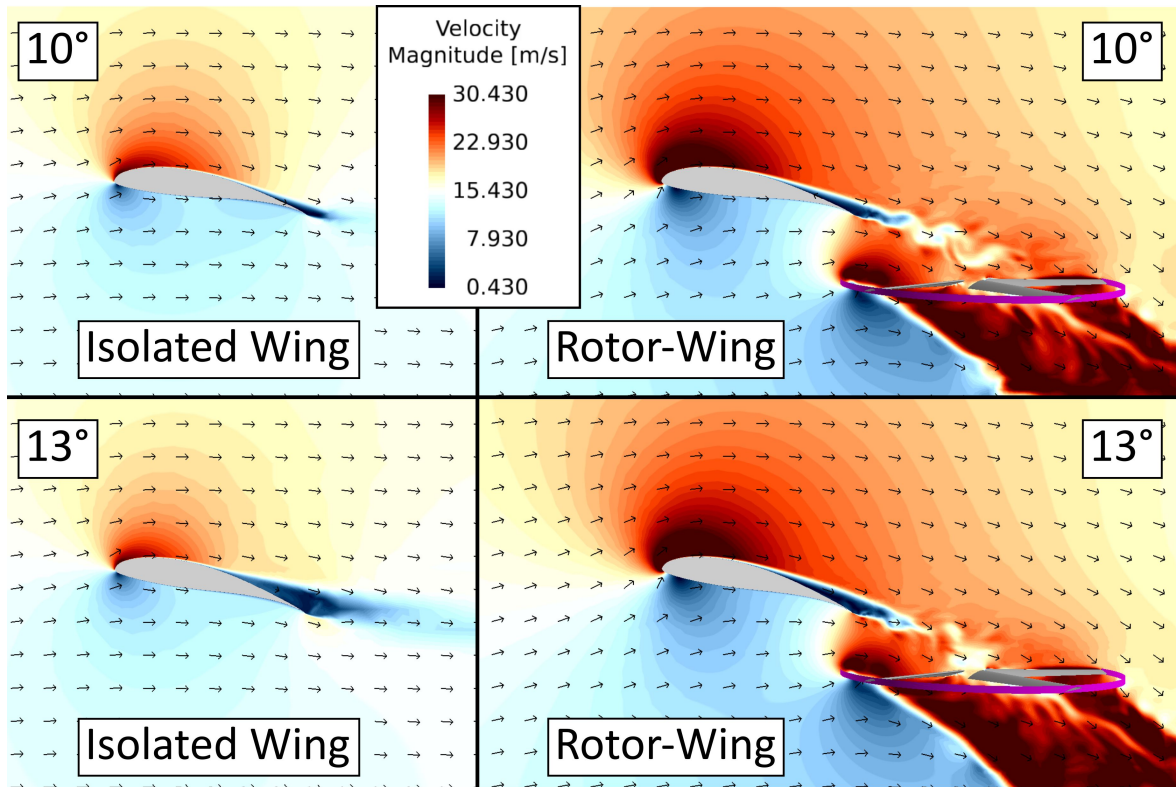


Figure 14: Instantaneous velocity magnitude slice cutting through the center of an isolated wing ($\alpha=10^\circ, 13^\circ$), and rotor-wing unit ($\alpha=10^\circ, 13^\circ$) with velocity vectors

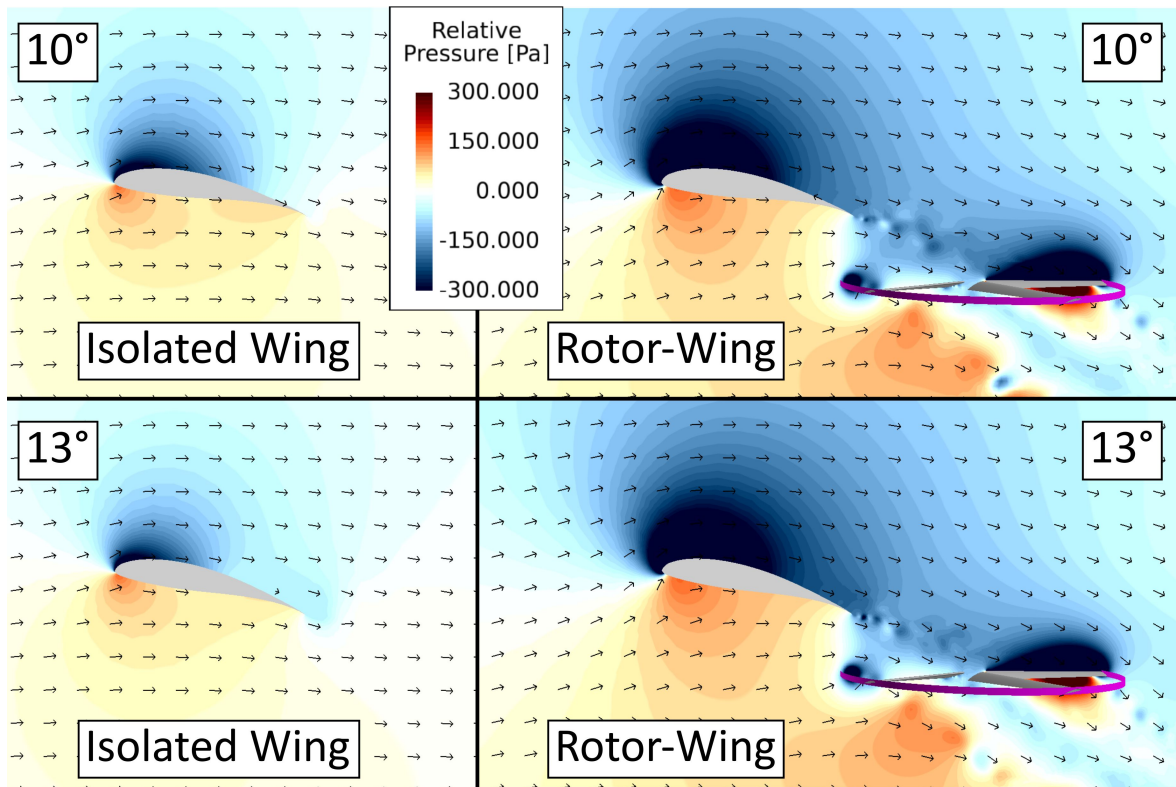


Figure 15: Instantaneous relative pressure slice cutting through the center of an isolated wing ($\alpha=10^\circ, 13^\circ$), and rotor-wing unit ($\alpha=10^\circ, 13^\circ$) with velocity vectors

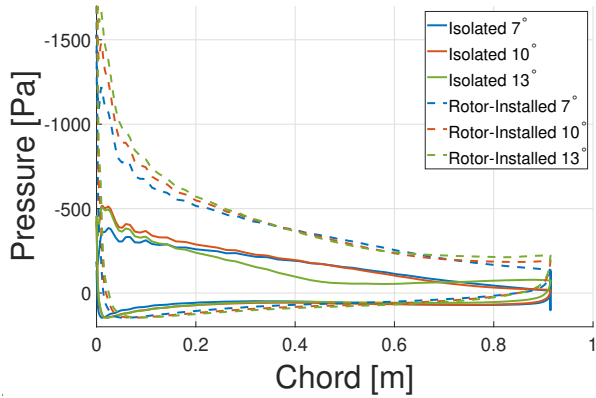


Figure 16: Chordwise relative pressure distribution along an isolated wing and rotor-installed wing at 7°, 10° and 13° incidence angle

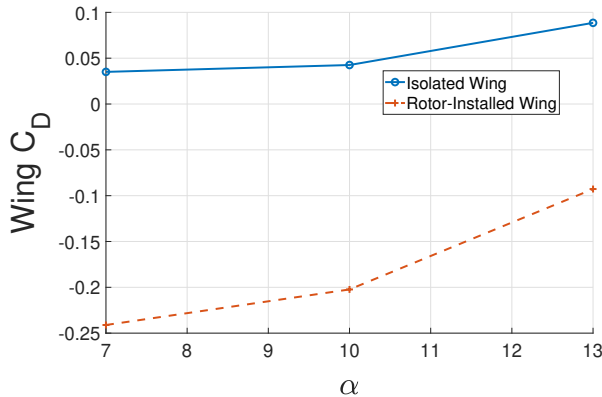


Figure 17: Wing drag coefficient vs. angle of attack for isolated and rotor-installed wings

over the entire chord. When only the drag-wise component of the pressure vector is plotted (bottom half of Fig. 18), the forwards-pointing vectors can be seen near the leading edge. These act over only a small portion of the wing which can be seen in Fig. 19 which plots the drag-wise pressure component over the chord of the isolated and rotor-installed wing at 7° incidence angle. Here, negative drag-wise pressure indicates a propulsive force on that section of the wing, and positive indicated drag. For the isolated wing, there exists propulsive forces near the wing’s leading edge (blue highlighted region on the left). When integrated, the blue propulsive force region in Fig. 19 in conjunction with the corresponding blue drag force region and skin friction drag results in a net drag on the isolated wing.

On the rotor-installed wing in Fig. 18, the increased top-surface suction (seen in Fig. 13) is manifest in longer vectors along the top surface of the wing. Stronger suction on the forwards facing part of the wing leads to longer drag-wise vectors on the rotor-installed wing compared to the isolated wing. The forward-facing vectors on the rotor-installed wing in Fig. 18 correspond to the orange propulsive force region in Fig. 19. This orange propulsive force region extends beyond that of the blue isolated rotor, and is larger in area than the corre-

sponding drag force region. The pressure-derived propulsive force is greater than the skin friction drag, resulting in a net propulsive force which is responsible for the negative drag coefficient presented in Fig. 17. At higher angles of attack, the drag coefficient magnitude reported in Fig. 17 reduces for rotor-installed wings. While the top surface suction remains largely the same across each angle of attack (Fig. 16), the component of the airfoil’s surface normal acting in the drag direction increases with angle of attack (the back surface gets steeper). Therefore, at high angles of attack, the drag-wise suction on the back of the airfoil starts to counter the propulsive suction near the leading edge, reducing the drag coefficient magnitude.

Overall, when the rotor is installed below and behind the wing, the wing lift is improved via rotor-induced suction on the top surface (Fig. 11). The increase in wing lift is relatively insensitive to angle of attack, and even provides some stall mitigation at high angles (Fig. 9). The added suction extends to the leading edge of the wing (Fig. 16), inducing a propulsive force on parts of the wing pointing upstream (Fig. 18). With the increased wing lift and negative drag, the presence of a nearby below-behind rotor provides a net performance improvement to the wing. However, wing performance is only half of the equation (in this case the equation being Eq. 1). The wing’s influence on the rotor also plays a part in overall L_{Tot}/D_{e-Tot} (Fig. 8).

Rotor Performance

As a point of comparison, Fig. 20 presents the sectional thrust coefficient (dC_T/dx) distribution over the isolated rotor operating in 30kts edgewise flight. Thrust is biased towards the advancing side of the disk due to the higher dynamic pressure and fixed blade pitch. Thrust is also skewed towards the front half of the disk due to longitudinal inflow variation (Ref. 40), with peak thrust being generated at $\psi = 120^\circ$.

When this rotor is installed below and behind a wing, the aerodynamic interference generated by the wing modifies the nominal thrust distribution. This is shown in Fig. 21 which plots the sectional thrust coefficient difference ($\Delta dC_T/dx$) between a wing-installed rotor (wing at 7°) and an isolated rotor (installed minus isolated). Here, blue represents a thrust deficit due to installation effects, and red indicates a thrust increment. In this case, the majority of the thrust difference is generated on the front of the disk, where an arc of thrust deficit is observed between $\psi = 90^\circ$ and $\psi = 270^\circ$. The operating condition (flight speed, rotor RPM, blade pitch, rotor angle) is identical between the wing-installed rotor and the isolated rotor, leaving only rotor installation effects responsible for the thrust deficit.

Fig. 22 shows the vertical velocity induced by an isolated 7° wing on the area that would be occupied by a below-behind rotor (no rotor actually simulated here). The wing is plotted in gray, and the perimeter of the rotor disk is annotated in magenta. Blue represents downwash, which is seen to be induced by the wing on the entire rotor disk. Downwash is strongest at

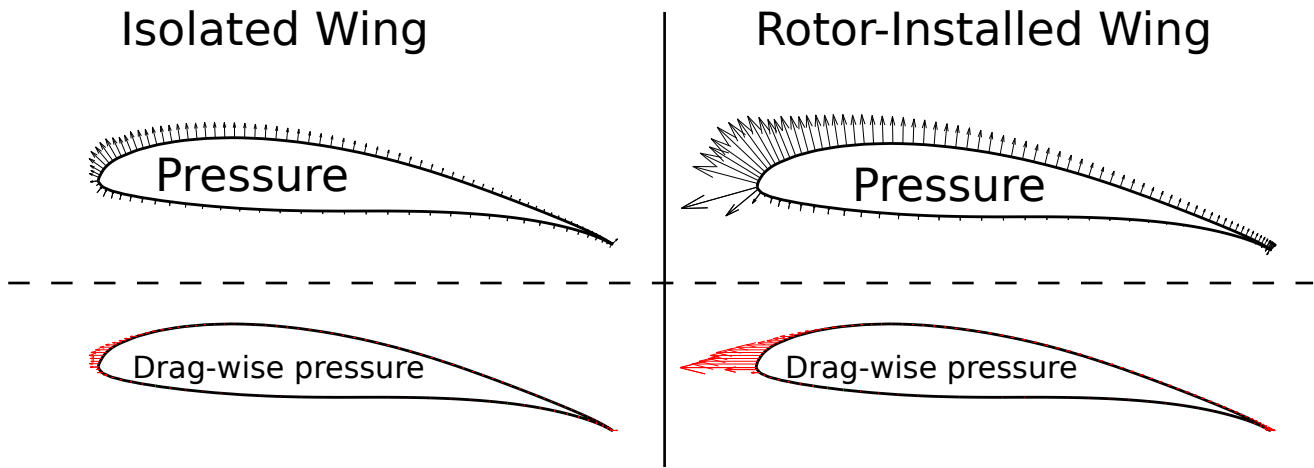


Figure 18: Surface-normal vectors along isolated and rotor-installed wings at 7° incidence, with vector lengths scaled to the surface pressure. The drag-wise component of these vectors is also included for each wing

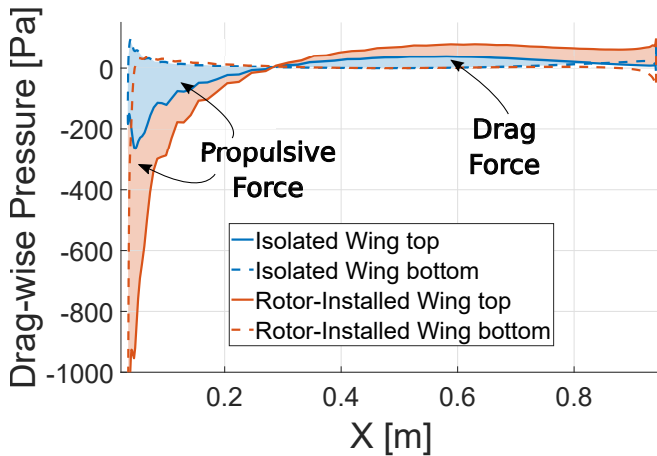


Figure 19: Drag-wise pressure component on the 7° isolated and rotor-installed wing (pressure multiplied by the surface-normal vector's x-component)

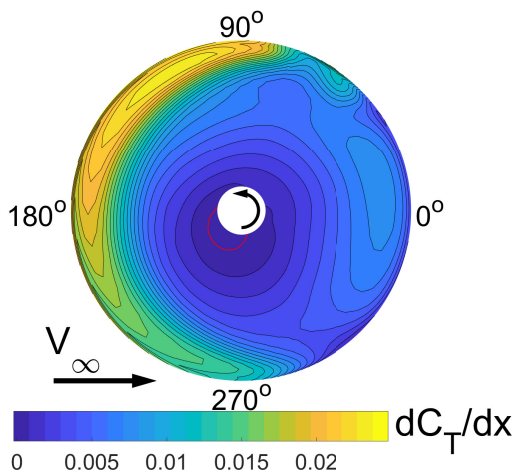


Figure 20: Sectional thrust coefficient dC_T/dx over the disk of an isolated rotor in 30 kts edgewise flight at a target 9 lb/ft^2 disk loading

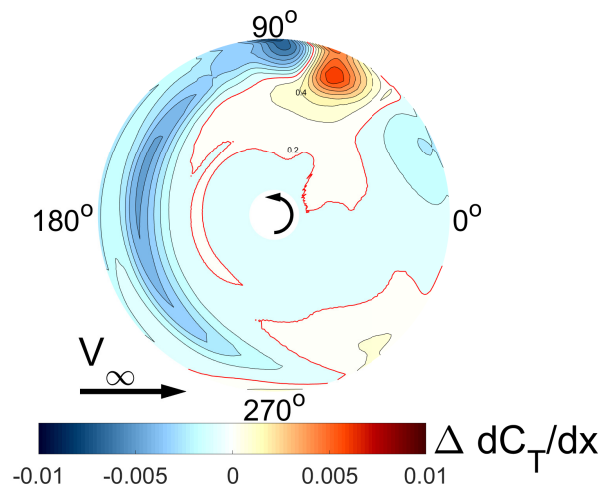


Figure 21: Sectional thrust coefficient difference $\Delta dC_T/dx$ between a rotor installed below and behind a 7° wing and an isolated rotor (installed minus isolated), both operating in 30 kts edgewise flight at a target 9 lb/ft^2 disk loading

the front of the disk and reduces towards the back of the disk that is positioned farther away from the wing. This downwash distribution is consistent with the wing's bound circulation, which induces downwash behind the wing and upwash in front of the wing. The downwash at the front of the disk is also consistent with the majority of the thrust deficit in Fig. 21. From a blade element theory perspective, downwash on a blade will increase the local inflow angle, thereby reducing the aerodynamic angle of attack and the generated lift. Therefore, it can be concluded that the downwash induced by the wing's bound circulation is responsible for the thrust deficit observed on the front of the rotor.

The overall performance metrics for the isolated and installed rotors are presented in Table 4. The rotor metrics are the same as those used in Eq. 1, namely rotor thrust L_R , H-force D_R , torque Q_R , rotation rate Ω , flight speed V_∞ and equivalent

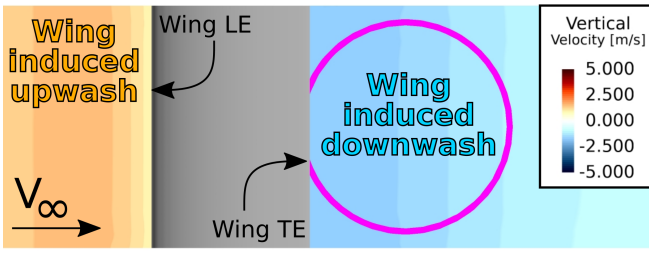


Figure 22: Slice cutting through the position of a below-behind rotor colored by the vertical velocity of an isolated 7° wing as viewed from the top

drag ratio L_R/D_{e-R} . Out of all four cases, the isolated rotor thrust is the greatest, with wing interactions imposing a thrust deficit on wing-installed rotors. Wing installation penalties are weakest when the wing is at 7° (93.3% nominal thrust), and grow stronger as the wing angle is increased (89.9% nominal thrust at 13°). Rotor H-force reduces when the wing is installed, dropping by up to 8.9% (at 10° wing angle). However, compared to the torque component ($Q_R\Omega/V_\infty$), rotor H-force contributes only a small fraction to the overall equivalent drag. For all four cases, the torque component $Q_R\Omega/V_\infty$ is on the order of 25 times the H-force and dominates the denominator of L_R/D_{e-R} at this low 30 kts operating speed. Comparing between cases, the torque required by the installed rotors is up to 4.3% greater than that required by the isolated rotor. Overall, the equivalent lift to drag ratio of all four rotors is relatively low, owing to the slow 30kts flight speed and high 9 lb/ft² disk loading. For the wing-installed rotors, interactional aerodynamics reduce L_R/D_{e-R} by introducing a thrust deficit and torque increment. Installation penalties increase with wing angle as the bound circulation increases, thereby strengthening the wing-induced velocity. In particular, the relative L_R/D_{e-R} deficit between wing-installed rotors and the isolated rotor ranges from 8.7% at 7° wing angle to 13.9% at 13° wing angle. While wing performance was shown to strongly improve in the presence of the rotor, it is apparent that this benefit does come at a modest cost to rotor performance.

Table 4: Rotor performance metrics for isolated and wing-installed rotors

	L_R [N]	D_R [N]	$\frac{Q_R\Omega}{V_\infty}$	$\frac{L_R}{D_{e-R}}$
Isolated Rotor	587	22.4	488	1.15
7° Wing-installed Rotor	548	21.2	503	1.05
10° Wing-installed Rotor	528	20.4	499	1.02
13° Wing-installed rotor	527	20.7	509	0.99

System Performance

In the rotor-wing system, interactional aerodynamics between the components have been shown to produce both performance improvements for the wing and performance deficits for the rotor. An evaluation of the total system performance must be conducted in order to evaluate the merits of each con-

figuration. Table 5 provides wing and rotor performance metrics for the rotor-wing units at each wing angle. As a point of comparison, interaction-free rotor-wing systems are also included by combining the performance of isolated wings with those of an isolated rotor. The first set of columns present wing performance metrics: wing lift L_W and drag D_W . The second set of columns give the same rotor performance metrics from Table 4, and the final set gives the total lift L_{Tot} , drag D_{Tot} , and equivalent lift to drag ratio L_{Tot}/D_{Tot} from Eq. 1.

Comparing wing lift L_W to rotor thrust L_R , the lift share without wing-rotor interaction (Isolated 7°, 10° and 13° cases) is on the order of 2:1 in favor of the rotor. However, when wing-rotor interaction is introduced, suction from the rotor introduces increased wing lift to 51% of the total lift at 7°, 53.5% at 10° and 55% at 13° wing incidence. Without wing-rotor interaction, the 13° wing would only produce 32.0% of the overall lift. Compared to the rotor thrust deficit, the wing lift increment is dominant, driving the total lifting force L_{Tot} 26.5-35.7% higher for the units with interaction versus those without.

The improved wing lift does not come at the penalty of wing drag, in fact the rotor-wing interaction introduces a propulsive force on the wing that is particularly strong at low wing angles. However, it does come at the cost of additional rotor torque (included in $Q_R\Omega/V_\infty$), which dominates D_{e-Tot} . The torque component of equivalent drag ($Q_R\Omega/V_\infty$) is 13-17 times greater than the other D_{e-Tot} components ($D_W + D_R$) both with and without interaction effects. With interaction, aerodynamic interference from the wing increases torque-related drag for the with-interaction cases, but this is countered by the introduction of propulsive force on the wing. Particularly at low wing angles (7° and 10° Wing-Rotor Units), the propulsive force from the wing counters the additional $Q_R\Omega/V_\infty$, leading to a lower total drag than if no interaction were present. While $Q_R\Omega/V_\infty$ may dominate D_{e-Tot} , the additional torque induced by wing-rotor interaction is less than the swing in wing drag, leading to a net drag deficit for with-interaction cases.

The net lift increment in conjunction with the net drag improvement leads to an overall L_{Tot}/D_{e-Tot} improvement for with-interaction cases. Isolated cases without interaction produce a relatively low L_{Tot}/D_{e-Tot} largely due to the low operating speed (30 kts). Interaction effects improve the nominal L_{Tot}/D_{e-Tot} by 34-40% largely due to the 26.5-35.7% total lift increase, but also in part due to the 2.7-7.0% total drag reduction. Performance improvements are also found to be relatively insensitive to wing angle. This is because the wing lift increment is caused by rotor-induced suction on the wing's top surface and not because of stall mitigation as was originally hypothesized. The rotor performance penalty associated with interactional effects is also found to be less significant than the wing's performance improvement. Overall, at the considered flight conditions, wing-rotor interaction is shown to dramatically improve overall system performance, regardless of the wing angle tested.

Table 5: Wing, rotor and rotor-wing unit performance metrics

	L_W [N]	D_W [N]	L_R [N]	D_R [N]	$\frac{Q_{R\Omega}}{V_\infty}$	L_{Tot}	D_{e-Tot}	$\frac{L_{Tot}}{D_{e-Tot}}$
7° Without Interaction	295	6.41	587	22.4	488	882	517	1.71
10° Without Interaction	320	7.78	587	22.4	488	908	518	1.75
13° Without Interaction	276	16.2	587	22.4	488	863	527	1.64
7° With Interaction	568	-44.1	548	21.2	503	1116	481	2.32
10° With Interaction	607	-37.0	528	20.4	499	1135	482	2.35
13° With Interaction	645	-17.0	527	20.7	509	1171	513	2.29

Disk Loading Effects

The performance improvements afforded by wing-rotor interaction are in large part reliant on the suction produced by the rotor. The suction that the rotor induces on the wing's top surface will be effected by the rotor's operating condition, namely the disk loading. In order to test what role disk loading has on rotor-wing interactions, two additional rotor-wing units are simulated at 6 lb/ft² and 12 lb/ft². The wing angle for these cases is kept at 7°, leaving a total of three disk loadings at this wing angle: 6, 9 and 12 lb/ft².

The effect of disk loading on wing lift is investigated first. Fig. 23 shows isolated and rotor-installed wing lift at each disk loading considered. The isolated wing lift in the absence of the rotor is also plotted for reference. When the rotor is installed, the wing's lift coefficient is shown to increase linearly with disk loading. At the nominal 9 lb/ft² disk loading, wing lift is improved by 92.5%, but at 6 lb/ft², that increment is dropped to 66.8%, and at 12 lb/ft², the increment improves to 116%. The slope of this curve indicates that C_L increases by 0.132 for every additional lb/ft² disk loading, however this would leave C_L at 1.89 with the rotor off (0 lb/ft²), which is above the nominal 1.61. This suggests that the C_L increment introduced by the rotor may actually have a nonlinear variation over a larger disk loading range (it may have more variation at lower disk loadings). Within this disk loading range, though, it is confirmed that the wing lift increment is sensitive to the rotor's disk loading.

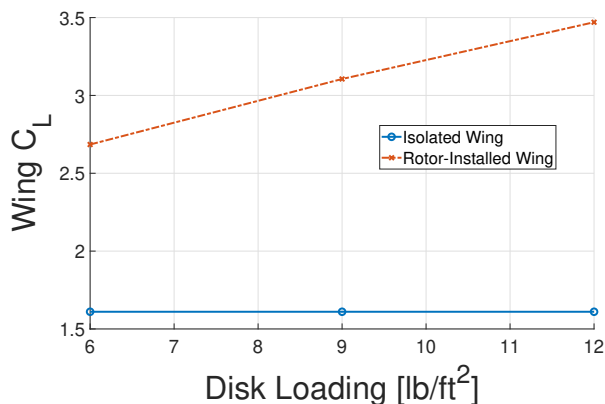


Figure 23: Wing lift coefficient vs. disk loading for isolated and rotor-installed wings

Like in Fig. 11, the wing lift increment can be tied to the suction produced by the rotor. When the rotor's disk loading is increased, it's suction effect is strengthened, which can be seen in Fig. 24. On the left panel, a slice cutting through the rotor hub is viewed from the left side colored by the difference in pressure between when the rotor operates at 6 lb/ft² versus the nominal 9 lb/ft² (6 lb/ft² minus 9 lb/ft²). Red indicates that the unit with a 6 lb/ft² rotor is producing higher relative pressure, and blue indicates that it is producing a lower relative pressure. Velocity vectors are also included, with black vectors indicating the velocity direction when the rotor operates at the nominal 9 lb/ft². The right half of the panel denotes the same slice, but colored by the pressure difference between when the rotor operates at 12 lb/ft² and 9 lb/ft² (12 lb/ft² minus 9 lb/ft²). Again, black velocity vectors for the 9 lb/ft² case are also included.

On the left side of Fig. 24, predominantly orange and red are observed above the rotor and wing, indicating that pressure is higher in this area when the rotor operates at 6 lb/ft². This region is associated with negative relative pressure (blue in Fig. 11), so the 6 lb/ft² rotor is inducing weaker suction on the top surface of the wing. This is especially true near the leading edge of the wing, where dark red is observed. This is indicative of the suction in this region being more than 100 Pa weaker at the lower 6 lb/ft² disk loading than the nominal 9 lb/ft². Weaker suction on the top surface of the wing can be expected to reduce the wing's lift increment seen in Fig. 9, and weaker suction near the leading edge will detriment the net propulsive force observed in Fig. 17.

While reducing the rotor's disk loading is shown to weaken the suction over the wing, increasing the disk loading has the opposite effect. On the right half of Fig. 24, blue is observed over the rotor and the wing, indicating increased suction at 12 lb/ft² relative to the nominal 9 lb/ft². Where the 6 lb/ft² rotor induced less suction near the leading edge of the wing, the 12 lb/ft² rotor induces in excess of 100 Pa greater suction. Below the wing, the pressure difference is insignificant, indicating that the pressure in this region is insensitive to the rotor's disk loading. This suggests that the placement of the rotor is such that rotor suction is only induced on the top of the wing, where it is beneficial to lift production, and not on the bottom surface where it could be detrimental.

The top surface pressure's sensitivity to disk loading can also be seen in Fig. 25 which compares the wing pressure distribution for rotor-wing units at 6, 9 and 12 lb/ft². The pressure distribution of an isolated wing is also plotted for reference.

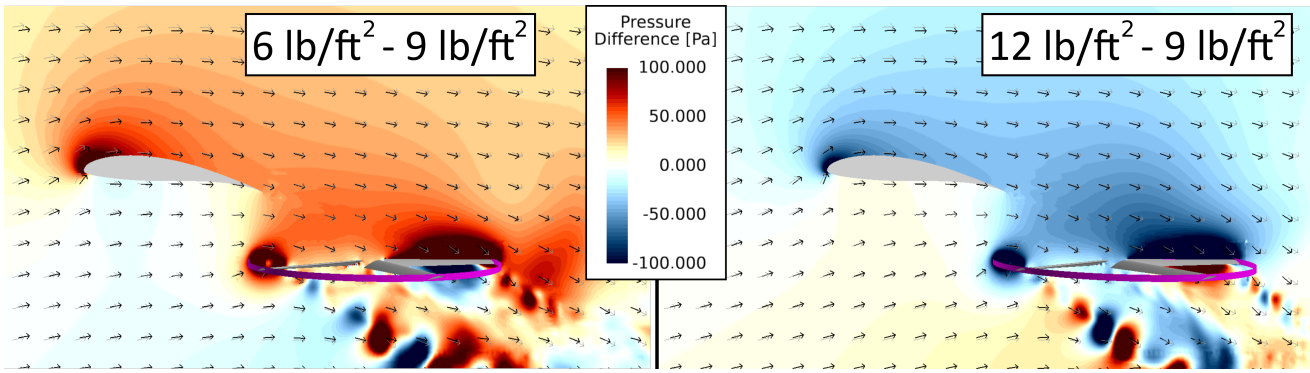


Figure 24: Side view of a slice cutting through the center of a rotor-wing unit ($\alpha=7^\circ$) colored by the difference in pressure between when the rotor is at 6 lb/ft² and 9 lb/ft². A second slice denotes the pressure difference between the rotor at 12 lb/ft² and 9 lb/ft²

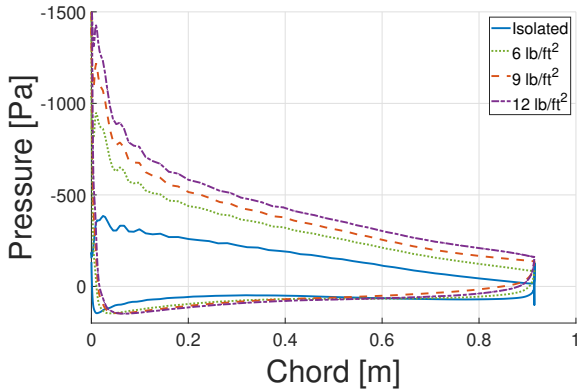


Figure 25: Chordwise relative pressure distribution along an isolated wing and rotor-installed wing with the rotor at 6, 9 and 12 lb/ft² disk loading

At all three disk loadings, the rotor induces additional suction on the top surface of the wing. When the rotor operates at a lower than nominal disk loading (6 lb/ft²), the top surface suction reduces by 42-270 Pa. When instead, the rotor's disk loading is increased to 12 lb/ft², the top surface suction strengthens by 47-208 Pa. Changes in top surface pressure are relatively constant from the trailing edge to about 22% chord, and then increase near the leading edge, where the nominal rotor-induced suction is high.

When the suction near the wing leading edge increases with disk loading, so too does the propulsive force generated by the wing. Fig. 26 presents the wing's drag coefficient vs. rotor disk loading, with the drag coefficient of the isolated wing included for reference. As disk loading is increased, the suction induced near the leading edge of the wing strengthens, and the propulsive force generated by the wing increases. The propulsive force increment observed between 6 lb/ft² and 9 lb/ft² is greater than that seen between 9 lb/ft² and 12 lb/ft², indicating additional disk loading increases beyond 12 lb/ft² may provide diminishing returns (in terms of propulsive force). Nonetheless, the rotor disk loading has been shown to be positively correlated with the wing's propulsive force.

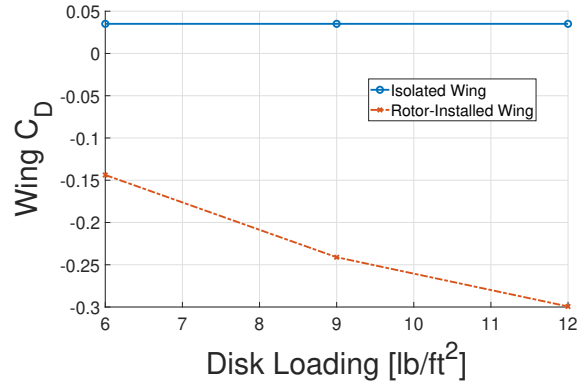


Figure 26: Wing drag coefficient vs. rotor disk loading for isolated and rotor-installed wings

Increasing the rotor disk loading has been shown to increase the wing lift increment as well as the wing propulsive force. These trends also inform the overall system performance, which is reported in Table 6. The same wing and rotor performance metrics as Table 5 are reported here, this time for rotor-wing units at varying rotor disk loading both with and without interactional effects. Comparing lift components, L_W for the with-interaction cases is positively correlated with disk loading, providing lift increments ranging 66.4% - 115% as previously seen in Fig. 23. Rotor thrust naturally also increases with disk loading, and with-interaction cases show a relatively consistent 5-6% thrust deficit compared to without-interaction cases. This thrust deficit can be seen graphically in Fig. 27 which presents wing lift and rotor thrust at each disk loading both with and without interaction effects. Without interaction, only rotor thrust is sensitive to disk loading, and so total system thrust's sensitivity to disk loading will be identical to that of the isolated rotor. Due to interaction, the wing lift is increased substantially, while the rotor thrust shows a modest reduction, and both depend on rotor disk loading. At low disk loading (below 9 lb/ft²), the wing lift is greater than the rotor thrust, but above 9 lb/ft² this trend is reversed.

In terms of drag, the propulsive force produced by the rotor-

Table 6: Wing, rotor and rotor-wing unit performance metrics at varying disk loading

	L_W [N]	D_W [N]	L_R [N]	D_R [N]	$\frac{Q_R \Omega}{V_\infty}$	L_{Tot}	D_{e-Tot}	$\frac{L_{Tot}}{D_{e-Tot}}$
6 lb/ft ² Without Interaction	295	6.41	393	16.3	248	687	271	2.53
9 lb/ft ² Without Interaction	295	6.41	587	22.4	488	882	517	1.71
12 lb/ft ² Without Interaction	295	6.41	773	27.4	764	1067	798	1.34
6 lb/ft ² With Interaction	491	-26.30	373	17.0	268	864	259	3.34
9 lb/ft ² With Interaction	568	-44.10	548	21.2	503	1116	481	2.32
12 lb/ft ² With Interaction	635	-54.75	725	24.6	772	1359	741	1.83

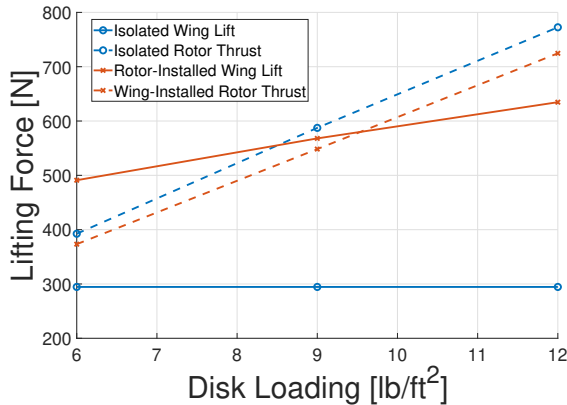


Figure 27: Wing lift L_W and rotor thrust L_R vs. disk loading for isolated rotors and wings (without interaction) and rotor-wing units (with interaction)

installed wings strengthens with disk loading (as seen in Fig. 26), but these forces are small compared to rotor $Q_R \Omega / V_\infty$ which increases with disk loading. Not only is the rotor $Q_R \Omega / V_\infty$ 9.3-26.9 times greater than the wing drag, but it is also much more sensitive to disk loading as can be seen in Fig. 28. This figure presents the components of D_{e-Tot} at each disk loading both with and without interaction effects. Here, it can be seen that when interactions are included, the 1.0% - 8.1% torque penalty is countered by the wing's propulsive force (see Table 6). Total equivalent drag increases with disk loading both with and without interaction largely due to the increment in rotor torque.

Both with and without interaction effects, L_{Tot} / D_{e-Tot} degrades with disk loading which can be seen in Table 6. These trends are presented graphically in Fig. 29 which plots L_{Tot} / D_{e-Tot} at each disk loading for systems with and without interaction effects. The L_{Tot} / D_{e-Tot} component most sensitive to disk loading is the rotor itself. The rotor-only L_R / D_{e-R} is presented in Fig. 30, and decreases with disk loading both with and without wing interactions. This downward trend in rotor performance explains why L_{Tot} / D_{e-Tot} in Fig. 29 reduces with disk loading.

Considering aerodynamic interactions, rotor-wing interference introduces a rotor thrust deficit (Fig. 27) and torque penalty (Fig. 28) at all disk loadings. These rotor performance penalties are manifest in Fig. 30 where the $\Delta L_R / D_{e-R}$ ranges from 11.5% at 6 lb/ft² down to 6.8% at 12 lb/ft², indicating the rotor performance is more robust to interactional effects at high disk loading.

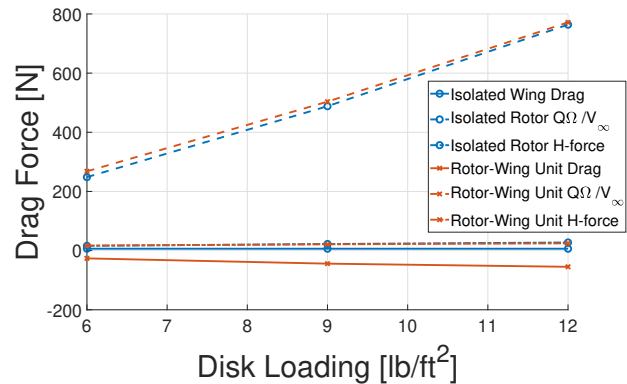


Figure 28: Wing drag D_W , rotor H-force D_R and equivalent drag $Q \Omega / V_\infty$ vs. disk loading for isolated rotors and wings (without interaction) and rotor-wing units (with interaction)

Despite rotor performance penalties, the wing lift increments associated with aerodynamic interaction induce improved L_{Tot} / D_{e-Tot} at all disk loadings. These improvements are more pronounced at lower disk loading ($\Delta L_{Tot} / D_{e-Tot} = 0.81$ at 6 lb/ft² and 0.49 at 12 lb/ft²) in part because wing lift increments contribute more to total system performance when the wing shares more of the total lift. It is the wing that provides interaction-related performance improvements, and so units in which the wing provides a greater fraction of overall lift benefit more from rotor-wing interaction.

Overall, disk loading affects rotor-wing system performance in two ways. As disk loading increases, stronger rotor suction induces additional wing lift increment. Simultaneously, increased disk loading is associated with reduced rotor performance. The reduced rotor performance brings down L_{Tot} / D_{e-Tot} at high disk loading regardless of whether interactions are included. When interactions are included, the wing lift increment is most beneficial at low disk loading where the wing lift share is greatest (despite weak rotor suction and relatively small wing lift increment). Even though performance is improved most at low disk loading, aerodynamic interactions benefit system performance at all disk loadings considered and provide at minimum 32% higher L_{Tot} / D_{e-Tot} compared to without-interaction cases.

DISCUSSION AND FUTURE WORK

These results suggest that at low flight speeds, a rotor mounted below and behind the wing can supplement total lift not only

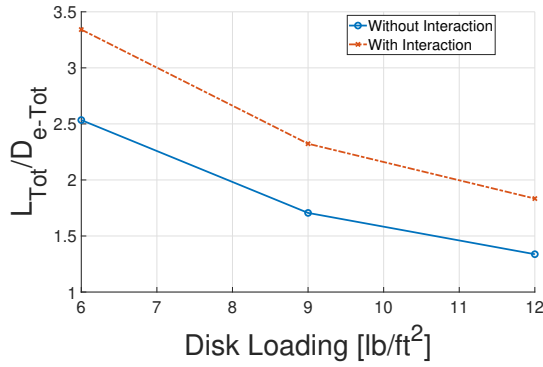


Figure 29: Total system equivalent lift to drag ratio L_{Tot}/D_{e-Tot} vs. disk loading for rotor-wing systems with and without aerodynamic interactions

by introducing its own thrust, but by also augmenting the wing lift. For a given vehicle lift requirement, this wing lift augmentation allows for the rotor thrust to be reduced (thereby lessening the power required and improving L_{Tot}/D_{e-Tot}). By mounting the rotor below and behind the wing, the interactional aerodynamics can provide improved vehicle performance, at least under low-speed/transition conditions where rotor power is dominant, but there is still enough dynamic pressure for the wing to share the total lift required. In a military context, performance in these conditions will be important for loiter and reconnaissance missions, whereas in an urban air mobility context, these benefits would more likely be realized during final approach or during a short-term holding pattern.

Beyond these circumstances, it remains to be seen whether a rotor mounted below and behind the wing can provide performance improvement at higher speeds more akin to a cruise condition. As V_∞ grows, $Q_R\Omega/V_\infty$ will drop while the nominal wing drag rises. If the aerodynamic interactions at higher speeds still provide a wing lift increment and drag deficit, the L_{Tot}/D_{e-Tot} improvements could be even higher than those reported in Tab. 5 and 6, since $Q_R\Omega/V_\infty$ will no longer be the dominant denominator term. Performance improvements at high speeds are particularly relevant to eVTOL vehicles as a majority of their mission time is consumed by cruise segments. For these vehicles, many of which already employ lifting rotors mounted to a wing, positioning the rotors below and behind the wing has the potential to enable enhanced forward flight efficiency.

CONCLUSIONS

This study investigates the aerodynamic interactions of a rotor-wing unit where the lifting rotor is mounted below and behind the wing. The computational fluid dynamics code AcuSolve[®] with DDES, is used to simulate the aerodynamics of the system and predict the rotor and wing performance both with and without interactions. Symmetry boundary conditions are used on either side of the wing section to emulate the presence of adjacent rotor-wing units along the wing span,

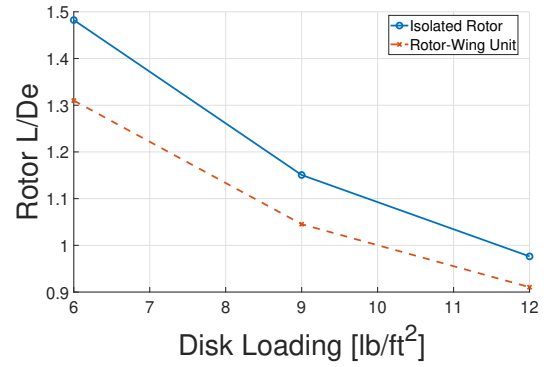


Figure 30: Rotor equivalent lift to drag ratio L_R/D_{e-R} vs. disk loading for an isolated rotor (without interaction) and a wing-installed rotor (with interaction)

and the sliding mesh method is used to simulate blade motion. The five bladed, 4 ft diameter rotors operate in 30 kts edge-wise flow and are positioned 0.7R below and 2R behind the quarter-chord of the wing, which is defined as a FX 63-137 airfoil with a 3 ft chord. In all, eleven cases are simulated: isolated rotors at 6, 9 and 12 lb/ft² disk loading, isolated wings at 7°, 10° and 13° incidence angle, rotor-wing units at 7°, 10° and 13° incidence angle (at 9 lb/ft² DL), and rotor-wing units at 6, 9, and 12 lb/ft² disk loading (with the wing at 7° incidence). The aerodynamics and performance of the combined rotor-wing units are compared to their isolated rotor and wing counterparts in order to identify the effect of rotor-wing interaction. Through these comparisons, the following observations are made.

1. The lifting rotor mounted below and behind the wing induces additional suction over the top surface of the wing.
2. Rotor-induced suction on the top surface of the wing increases wing lift by up to 134%. This phenomena increases at higher values of rotor disk loading.
3. Added suction near the leading edge of the wing counters the nominal wing drag and introduces a net propulsive force. This increases at higher wing incidence angles and higher rotor disk loading.
4. Wing-induced downwash on the rotor introduces a thrust deficit of up to 10% and a torque penalty of up to 4% from the nominal.
5. Despite rotor performance penalties, the added wing lift and reduced wing drag introduced by aerodynamic interactions increases L_{Tot}/D_{e-Tot} for the unit by up to 49% compared to if no interactions were present.
6. As the rotor disk loading increases, rotor induced suction on the top surface of the wing grows stronger, increasing the wing lift coefficient by approximately 0.13 for each additional lb/ft² disk loading.

ACKNOWLEDGMENTS

The authors would like to thank Rensselaer Polytechnic Institute and the Center for Computational Innovations. The findings from this study are made possible thanks to the availability of their computing resources and dedicated staff that maintain the network and hardware.

REFERENCES

1. Misiorowski, M., Gandhi, F., and Oberai, A. A., "Computational Study on Rotor Interactional Effects for a Quadcopter in Edgewise Flight," *AIAA Journal*, Vol. 57, (12), 2019, pp. 5309–5319. DOI: 10.2514/1.J058369
2. Misiorowski, M., Gandhi, F., and Anusonti-Inthra, P., "Computational Analysis of Rotor-Blown-Wing for Electric Rotorcraft Applications," *AIAA Journal*, Vol. 58, (7), 2020, pp. 2921–2932. DOI: 10.2514/1.J058851
3. Healy, R., Misiorowski, M., and Gandhi, F., "A CFD-Based Examination of Rotor-Rotor Separation Effects on Interactional Aerodynamics for eVTOL Aircraft," *Journal of the American Helicopter Society*, Vol. 67, (1), January 2022, pp. 1–12. DOI: 10.4050/jahs.67.012006
4. Healy, R., Gandhi, F., and Mistry, M., "Computational Investigation of Multirotor Interactional Aerodynamics with Hub Lateral and Longitudinal Canting," *AIAA Journal*, Vol. 60, (2), February 2022, pp. 872–882. DOI: 10.2514/1.j060530
5. Ventura Diaz, P., and Yoon, S., "High-Fidelity Computational Aerodynamics of Multi-Rotor Unmanned Aerial Vehicles," 2018 AIAA Aerospace Sciences Meeting, January 2018. DOI: 10.2514/6.2018-1266
6. Yoon, S., Pulliam, T. H., and Chaderjian, N. M., "Simulations of XV-15 Rotor Flows in Hover Using OVERFLOW," AHS 5th Aeromechanics Specialists' Conference, San Francisco, CA, USA, Jan 2014.
7. Yoon, S., Lee, H. C., and Pulliam, T. H., "Computational Analysis of Multi-Rotor Flows," 54th AIAA Aerospace Sciences Meeting, January 2016. DOI: 10.2514/6.2016-0812
8. Yoon, S., Ventura Diaz, P., Boyd Jr., D. D., Chan, W. M., and Theodore, C. R., "Computational Aerodynamic Modeling of Small Quadcopter Vehicles," Proceedings of the 73rd Annual Forum, Fort Worth, TX, May 2017.
9. Glauert, H., "Airplane Propellers," *Aerodynamic Theory*, Springer Berlin Heidelberg, 1935, pp. 169–360. DOI: 10.1007/978-3-642-91487-4₃
10. Fage, A., and Collins, H. E., "An Investigation of the Mutual Interference of Two Model Airscrews and a Model of the Sopwith Dolphin Aeroplane," *Br. A.R.C R. and M.*, (572), 1919.
11. Kroo, I., "Propeller-wing Integration for Minimum Induced Loss," *Journal of Aircraft*, Vol. 23, (7), July 1986, pp. 561–565. DOI: 10.2514/3.45344
12. Veldhuis, L., "Review of Propeller-wing Aerodynamic Interference," 24th International Congress of the Aeronautical Sciences, Vol. 6, 2004.
13. Chiamonte, J. Y., Favier, D., Maresca, C., and Benneceur, S., "Aerodynamic Interaction Study of the Propeller/Wing Under Different Flow Configurations," *Journal of Aircraft*, Vol. 33, (1), January 1996, pp. 46–53. DOI: 10.2514/3.46901
14. Müller, L., Heinze, W., Kožulović, D., Hepperle, M., and Radespiel, R., "Aerodynamic Installation Effects of an Over-the-Wing Propeller on a High-Lift Configuration," *Journal of Aircraft*, Vol. 51, (1), January 2014, pp. 249–258. DOI: 10.2514/1.c032307
15. Fischer, J., and Ortun, B., "Simulation & Analysis of the Aerodynamic Interaction Between Distributed Propulsion and Wings," AHS Technical Meeting on Aeromechanics Design for Transformative Vertical Flight, 2018.
16. Stoll, A. M., Bevirt, J., Moore, M. D., Fredericks, W. J., and Borer, N. K., "Drag Reduction Through Distributed Electric Propulsion," 14th AIAA Aviation Technology, Integration, and Operations Conference, June 2014. DOI: 10.2514/6.2014-2851
17. Deere, K. A., Viken, J. K., Viken, S., Carter, M. B., Wiese, M., and Farr, N., "Computational Analysis of a Wing Designed for the X-57 Distributed Electric Propulsion Aircraft," 35th AIAA Applied Aerodynamics Conference, June 2017. DOI: 10.2514/6.2017-3923
18. Singh, R., Sirohi, J., and Hrishikenvan, V., "Common Research Configuration for Collaborative Advancement of Scalable VTOL UAS Technologies," 75th Annual Forum of the American Helicopter Society, 2019.
19. Hebbar, U., Sahni, O., and Gandhi, F., "Comparison of Numerical Modeling Approaches for Flow over a Wing with an Upstream Rotor," AIAA SCITECH 2022 Forum, January 2022. DOI: 10.2514/6.2022-1332
20. Hebbar, U. U., Gandhi, F., and Sahni, O., "Parametric Investigation of Flow over a Rotor-Blown Wing using High-fidelity Simulations," Proceedings of the 78th Annual Forum, May 2022.
21. Kitty Hawk, "Heaviside," <https://kittyhawk.aero/heaviside/>, Accessed October 2021.

22. Wisk, “Cora,” <http://www.cora.aero/>, Accessed October 2021.
23. Vertical Aerospace, “Vertical Aerospace VA-X4,” <https://vertical-aerospace.com/va-x4/>, Accessed October 2021.
24. Archer Aviation, “Archer Maker,” <https://www.archer.com/maker>, Accessed October 2021.
25. Beta Technologies, “Alia-250c,” <https://www.beta.team/aircraft/>, Accessed October 2021.
26. Joby Aviation, “Joby Aviation,” <https://www.jobyaviation.com/>, Accessed October 2021.
27. Fejtek, I., and Roberts, L., “Navier-Stokes Computation of Wing/Rotor Interaction for a Tilt Rotor in Hover,” *AIAA Journal*, Vol. 30, (11), November 1992, pp. 2595–2603. DOI: 10.2514/3.11272
28. Corle, E., Schmitz, S., and Floros, M., “Coupled CFD/CSD Predictions of Semi-Span XV-15,” AHS International Technical Meeting on Aeromechanics Design for Transformative Vertical Flight, January 2018.
29. Tran, S., Lim, J., Nunez, G., Wissink, A., and Bowen-Davies, G., “CFD Calculations of the XV-15 Tiltrotor During Transition,” 75th Annual Forum of the Vertical FLight Society, Philadelphia, PA, 2019.
30. Tang, E., and Chung, S.-J., “Experimental Studies of Propeller-Wing Interactions in Transition from Hover to Forward Flight,” AIAA SCITECH 2022 Forum, January 2022. DOI: 10.2514/6.2022-0018
31. Gandhi, F., Pepe, J., and Smith, B., “High Solidity, Low Tip-Speed Rotors for Reduced eVTOL Tonal Noise,” Proceedings of the 78th Annual Forum, May 2022.
32. Niemiec, R., and Gandhi, F., “Development and Validation of the Rensselaer Multicopter Analysis Code (RMAC): A Physics-based Low-fidelity Modeling Tool,” 75th Annual Forum of the Vertical FLight Society, Philadelphia, PA, 2019.
33. Airfoil Tools, <http://airfoiltools.com/>, 2022.
34. Drela, M., “XFOIL: An Analysis and Design System for Low Reynolds Number Airfoils,” , 1989, pp. 1–12. DOI: 10.1007/978-3-642-84010-4₁
35. ACUSIM Software, I., “AcuSolve Validation - NACA 0012 Airfoil,” Technical report, <http://altairhyperworks.com/ResourceLibrary.aspx?category=Case2010>, 2010.
36. Corson, D., Jaiman, R., and Shakib, F., “Industrial Application of RANS Modelling: Capabilities and Needs,” *International Journal of Computational Fluid Dynamics*, Vol. 23, (4), 2009, pp. 337–347. DOI: 10.1080/10618560902776810
37. ACUSIM Software, I., “AcuSolve Validation - Laminar to Turbulent Transition Over an Airfoil,” Technical report, <http://altairhyperworks.com/ResourceLibrary.aspx?category=Case2010>, 2010.
38. Jansen, K. E., Whiting, C. H., and Hulbert, G. M., “A Generalized- α Method for Integrating the Filtered Navier–Stokes Equations With a Stabilized Finite Element Method,” *Computer Methods in Applied Mechanics and Engineering*, Vol. 190, (3), 2000, pp. 305 – 319. DOI: [https://doi.org/10.1016/S0045-7825\(00\)00203-6](https://doi.org/10.1016/S0045-7825(00)00203-6)
39. N. Brooks, A., and J.R. Hughes, T., “Streamline Upwind/Petrov-Galerkin Formulations for Convection Dominated Flows with Particular Emphasis on the Incompressible Navier-Stokes Equations,” *Computer Methods in Applied Mechanics and Engineering*, Vol. 32, (1-3), 09 1982, pp. 199–259. DOI: 10.1016/0045-7825(82)90071-8
40. Niemiec, R., *Development and Application of a Medium-Fidelity Analysis Code for Multicopter Aerodynamics and Flight Mechanics*, Ph.D. thesis, Rensselaer Polytechnic Institute, August 2018.